

High-pressure polymorphs in Yamato-790729 L6 chondrite and their significance for collisional conditions

Yukako KATO¹, Toshimori SEKINE^{1,2}, Masahiko KAYAMA^{1,3}, Masaaki MIYAHARA ^{1,4*}, and Akira YAMAGUCHI ^{5,6}

¹Department of Earth and Planetary Systems Science, Graduate School of Science, Hiroshima University, Higashi-Hiroshima 739-8526, Japan

²Center for High Pressure Science and Technology Advanced Research, Shanghai 201203, China

³Creative Interdisciplinary Research Division, Frontier Research Institute for Interdisciplinary Sciences, Tohoku University, Sendai 980-8578, Japan

⁴Department of Earth and Planetary Materials Science, Graduate School of Science, Tohoku University, Sendai 980-8578, Japan

⁵National Institute of Polar Research, Tokyo 190-8518, Japan

⁶Department of Polar Science, School of Multidisciplinary Science, SOKENDAI (The Graduate University for Advanced Studies), Tokyo 190-8518, Japan

*Corresponding author. E-mail: miyahara@hiroshima-u.ac.jp

(Received 19 January 2017; revision accepted 07 August 2017)

HPSTAR
482-2017

Abstract—Shock pressure recorded in Yamato (Y)-790729, classified as L6 type ordinary chondrite, was evaluated based on high-pressure polymorph assemblages and cathodoluminescence (CL) spectra of maskelynite. The host-rock of Y-790729 consists mainly of olivine, low-Ca pyroxene, plagioclase, metallic Fe-Ni, and iron-sulfide with minor amounts of phosphate and chromite. A shock-melt vein was observed in the hostrock. Ringwoodite, majorite, akimotoite, lingunite, tuite, and xieite occurred in and around the shock-melt vein. The shock pressure in the shock-melt vein is about 14–23 GPa based on the phase equilibrium diagrams of high-pressure polymorphs. Some plagioclase portions in the host-rock occurred as maskelynite. Sixteen different CL spectra of maskelynite portions were deconvolved using three assigned emission components (centered at 2.95, 3.26, and 3.88 eV). The intensity of emission component at 2.95 eV was selected as a calibrated barometer to estimate shock pressure, and the results indicate pressures of about 11–19 GPa. The difference in pressure between the shock-melt vein and host-rock might suggest heterogeneous shock conditions. Assuming an average shock pressure of 18 GPa, the impact velocity of the parent-body of Y-790729 is calculated to be $\sim 1.90 \text{ km s}^{-1}$. The parent-body would be at least $\sim 10 \text{ km}$ in size based on the incoherent formation mechanism of ringwoodite in Y-790729.

INTRODUCTION

Planetesimal collision is one of the fundamental phenomena for the formation and evolution of the solar system. An asteroid was formed through accretion, collision, and subsequent reaccumulation of a planetesimal (e.g., Nakamura et al. 2011). Many meteorites originating from asteroids have suffered from impact events occurring on their parent-bodies; shock-

induced features, including melting textures and high-pressure polymorphs found in such meteorites, provide clear evidence for impact events. Of many ordinary chondrites, L6 type ordinary chondrite has a vein-like shock-induced melting texture, a shock-melt vein (or shock vein). The major constituents of ordinary chondrites are olivine, pyroxene, and plagioclase. These minerals entrained in or around the shock-melt veins transform into their high-pressure polymorphs due to

high-pressure and -temperature conditions induced by shock events (Chen et al. 1996; Ohtani et al. 2004; Xie et al. 2006; Ferroir et al. 2008; Ozawa et al. 2009, 2014; Tomioka et al. 2016). The high-pressure polymorphs formed in the shocked meteorites can be regarded as representatives of the deep Earth's interior materials. Accordingly, the formation processes of high-pressure polymorphs in shocked ordinary chondrites have been evaluated so far in detail, because they provide clues for understanding the physicochemical properties of the deep Earth's interior (e.g., Chen et al. 2007; Miyahara et al. 2010, 2013).

Shock pressure condition is one of the important parameters for clarifying the magnitude of an impact event because it gives an estimation of impact velocity based on the Rankine–Hugoniot equation. A shock stage classification system based on observations of the shock-recovered samples, mostly single minerals, has been used to estimate the shock pressure condition recorded in ordinary chondrites (Stöffler et al. 1991). However, the durations of shock pulse induced by shock experiments are too short (less than microseconds) compared to those of natural impact events (less than a few seconds) and the peak pressure in most recovered samples has been reached by multiple reflection of a shock wave. In addition, the formation kinetics of high-pressure polymorphs has not been considered in the shock stage classification system. Chen et al. (1996) proposed that high-pressure polymorph assemblages in the shock-melt veins allow us to estimate the shock pressure condition based on the phase equilibrium diagrams deduced by static high-pressure and -temperature synthetic experiments. Kayama et al. (2012) developed cathodoluminescence (CL) spectroscopy for estimating the shock pressure condition recorded in the maskelynite of shocked meteorites. Yamato-790729 L6 ordinary chondrite with a shock-melt vein is one of the heavily shocked ordinary chondrites. In this study, we applied both high-pressure polymorph assemblage and CL spectroscopy to estimate the shock pressure condition of Yamato-790729 L6, and compared the resultant shock pressure conditions to evaluate the validity of the methods.

MATERIALS AND EXPERIMENTAL METHODS

A petrographic thin section of an L6 ordinary chondrite, Yamato-790729 (hereafter, Y-790729), was obtained from the National Institute of Polar Research, Tokyo (NIPR) for this study. The petrographic thin section was observed under an optical microscope to describe its petrographic features first. A scanning electron microscope (SEM) equipped with an X-ray energy-dispersive spectrometer (EDS), JEOL JSM-

6390A, operating at an accelerating voltage of 15 kV, was employed for texture observations and phase identification at Hiroshima University. We also employed a field emission gun scanning electron microscope (FEG-SEM), JEOL JSM-7001F and 7100F, for fine textural observations at an accelerating voltage of 15 kV at Tohoku University and NIPR. Another SEM (JSM-5410) with a CL spectrometer was also used to characterize the shock metamorphic effects of feldspar and maskelynite in Y-790729. CL image was captured by a MiniCL system with highest sensitivity of total instrumental response in the UV-blue regions. CL spectra of maskelynite and plagioclase were obtained at a beam current of 2 nA under 10,000 magnification in the range of 300–800 nm by a step of 1 nm. All CL spectra obtained were corrected for the total instrumental response, which was calibrated based on a standard lamp (Kayama et al. 2010). Following the method reported by Stevens-Kalceff (2009) and Kayama et al. (2010), the corrected CL spectra were converted into energy unit scale, and then were deconvolved into Gaussian components. We referred previous data of maskelynite and crystalline feldspar to identify the number and peak position of Gaussian components and emission type (Kayama et al. 2010, 2012). A chi-squared test for CL spectral datum of each measured sample was also performed to fit in with the smallest margin of standard error.

The chemical compositions of the constituents were determined using a wavelength-dispersive electron micro-probe analyzer (EMPA), JEOL JXA-8200, installed at the N-BARD of Hiroshima University. Analyses were carried out using an accelerating voltage of 15 kV and beam currents and probe diameters of 15 nA and 3 μm for olivine and pyroxene, and 8 nA and 20 μm for lingunite, maskelynite, and plagioclase to reduce the loss of Na content during electron beam irradiation. Mineralogy was determined using a laser micro-Raman spectrometer, Renishaw inVia, installed at the Graduate School of Science, Hiroshima University. A microscope (objective: $\times 100$) was used to focus the excitation laser beam (a green laser, 532 nm line with 1800 L mm^{-1} grating). Laser power on a sample was kept at 7.5–15 mW. Acquisition times were 10–30 s. For each phase, a Raman shift was acquired in the spectral region of 300–1100 cm^{-1} .

A part of the sample was excavated with a focused ion beam (FIB) system, JEOL JEM-9320FIB, and a dedicated optical microscope with a manipulator installed at Tohoku University for transmission electron microscope (TEM) observation. A gallium ion beam was accelerated at 30 kV during sputtering of the slice by the FIB. The resultant slices were 100–130 nm in thickness. A JEOL JEM-2010 TEM, operating at

200 kV with a JEOL energy-dispersive X-ray spectroscopy (EDS) detector system at the N-BARD, was employed for conventional TEM observation and selected area electron diffraction (SAED) analysis. A JEOL JEM-2100F field emission TEM, operating at 200 kV with a JEOL EDS detector system at the Graduate School of Engineering of Tohoku University, was also employed for conventional TEM observation and SAED analysis. We determined the chemical composition of each mineral under a scanning TEM (STEM) mode with an EDS detector. The chemical compositions were corrected using experimentally determined k -factors (San Carlos olivine and pyrope were used as the known standards).

RESULTS

Petrography

The optical microscopic photograph of Y-790729 thin section under transmitted light is shown in Fig. 1. The Y-790729 is a typical L6 ordinary chondrite with the remnants of chondritic textures, and has a shock-melt vein with a width of $< \sim 620 \mu\text{m}$. Optical microscopic and SEM observations indicate that the host-rock of Y-790729 consists mainly of olivine, low-Ca pyroxene, plagioclase, metallic Fe-Ni, and iron-sulfide with minor amounts of phosphate and chromite. The olivine in the host-rock has a brownish staining and exhibits irregular fractures under transmitted light. Several brecciated low-Ca pyroxene and olivine grains were observed. Undulatory extinction was observed in some plagioclase and pyroxene grains.

High-Pressure Polymorphs of Olivine

Many mineral fragments (mainly olivine, low-Ca pyroxene, and plagioclase) are entrained in the shock-melt vein of Y-790729 (Figs. 2a–d). Many fine-grained dendritic crystals and spherical metallic iron-nickel-iron-sulfide assemblage grains with eutectic textures fill the interstices of the mineral fragments (Figs. 2e and 2f). Some fragments of large olivine (diameter about $100 \mu\text{m}$) entrained in the shock-melt vein are blue in color under a transmitted light microscope, suggesting that the portions have been transformed into a high-pressure polymorph, ringwoodite. Raman shifts for such portions appeared at ~ 798 and $\sim 843 \text{ cm}^{-1}$ (Fig. 3a), which is consistent with those for ringwoodite (Ohtani et al. 2004). Representative Raman shift for olivine is shown in Fig. 3b. EMPA analyses for these grains of olivine and ringwoodite indicate that both have almost same compositions (Table 1). Based on Raman analyses, most olivine grains entrained in the shock-melt

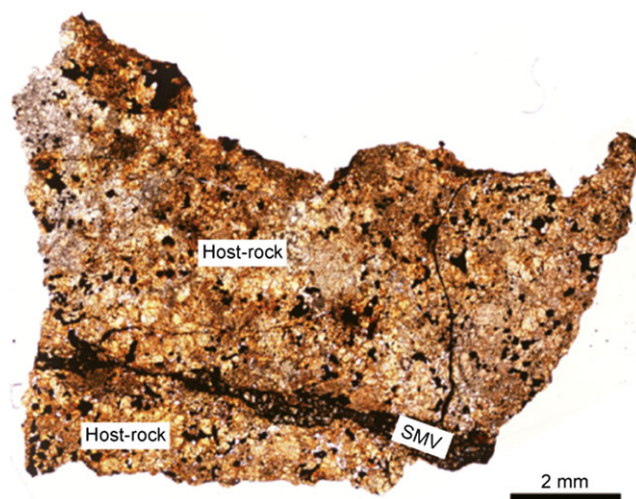


Fig. 1. The transmitted light photograph of Y-790729 studied here. SMV = shock-melt vein.

vein have been transformed into ringwoodite (Fig. 2a). Ringwoodite lamellae were observed in the olivine grain adjacent to the shock-melt vein (Fig. 2b). The texture of olivine grain replaced with ringwoodite near the shock-melt vein is different from that of olivine far from the shock-melt vein and similar to the olivine grain replaced with ringwoodite entrained in the shock-melt vein. The olivine grain replaced with ringwoodite entrained in the shock-melt vein was excavated by FIB and observed with a TEM (Figs. 2c and 2d). TEM images depict that the olivine is replaced with unoriented polycrystalline assemblage (Fig. 4a). Their grain sizes vary from $\sim 100 \text{ nm}$ to $\sim 1.3 \mu\text{m}$. The chemical compositions of individual ringwoodite grains were determined by STEM-EDS (Table 2), which are similar to those of the original olivine (Table 1).

High-Pressure Polymorphs of Pyroxene

Backscattered electron (BSE) images depict that fine-grained granular polycrystalline assemblages occur along the grain-boundaries or irregular fractures of low-Ca pyroxene grains entrained in the shock-melt vein (Fig. 2d). Some of the grains entrained in the shock-melt vein are replaced by fine-grained, needle-shaped polycrystalline assemblages (Fig. 2e). We observed four types of Raman spectra of pyroxene areas (Figs. 3f–i). Raman spectrum of the fine-grained granular polycrystalline assemblages are around ~ 594 , ~ 927 , and $\sim 1064 \text{ cm}^{-1}$ (Fig. 3f), which is diagnostic of majorite (McMillan et al. 1989; Ohtani et al. 2004). Raman spectra of the fine-grained, needle-shaped polycrystalline assemblages have peaks around ~ 798 , ~ 675 , ~ 478 , and $\sim 314 \text{ cm}^{-1}$ (Fig. 3h), which are diagnostic of

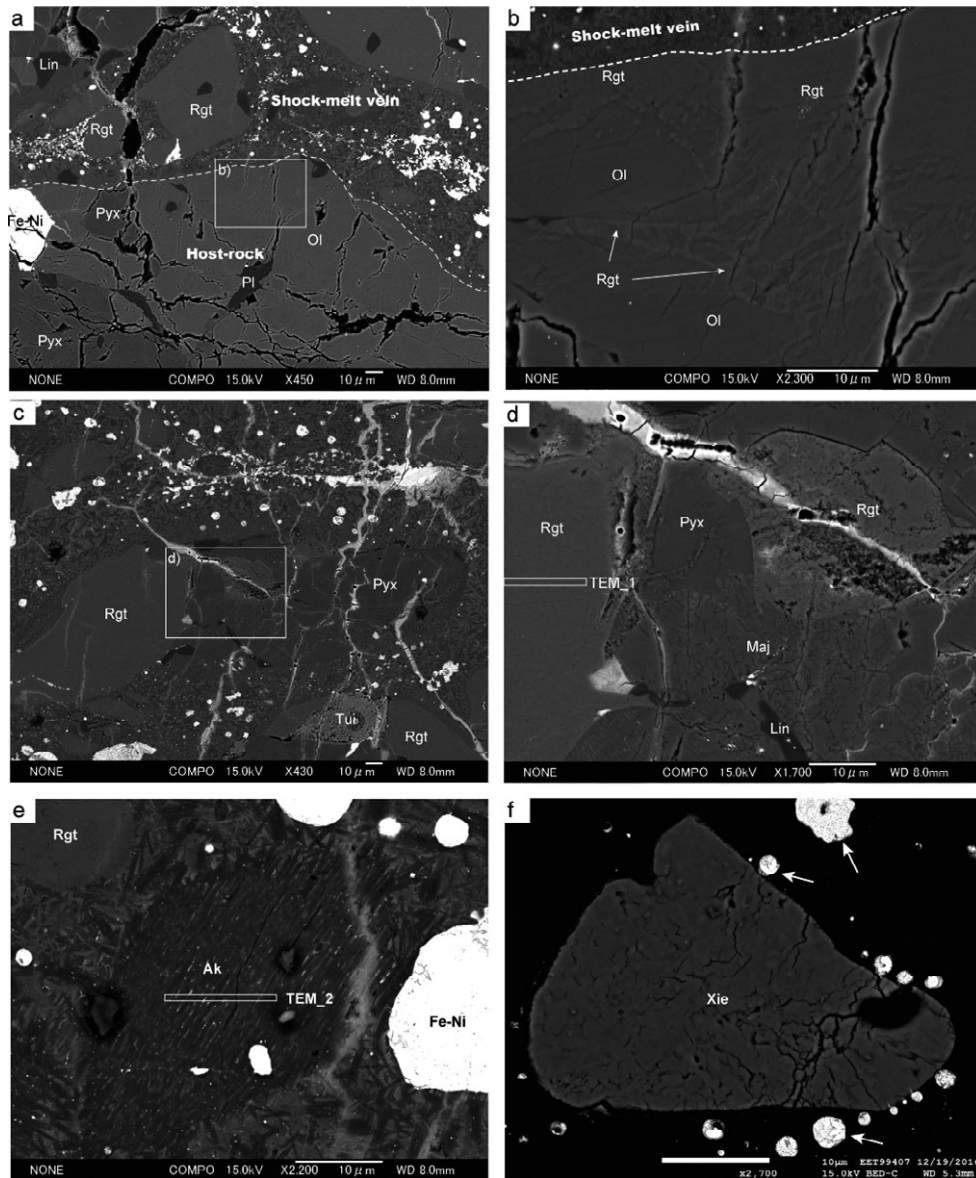


Fig. 2. Backscattered electron (BSE) images. a) Low-magnification image of the shock-melt vein of Y-790729 studied here. Many mineral fragments are entrained in the shock-melt vein. Original plagioclase (Pl) has transformed into lingunite (Lin). b) High-magnification image of the square at the center in (a). Olivine (Ol) near the shock-melt vein has transformed into ringwoodite (Rgt). c) Low-magnification image of mineral fragments entrained in the shock-melt vein. Original olivine has been completely replaced with Rgt. Original apatite has transformed into tuite (Tui). d) High-magnification image of the square at the center in (c). Low-Ca pyroxene (Pyx) has been partly replaced with majorite (Maj). e) Several low-Ca pyroxene grains have been replaced with fine-grained, needle-shaped polycrystalline akimotoite (Ak) assemblages. Fine-grained dendritic crystals occur around the polycrystalline Ak assemblages (the matrix portion of the shock-melt vein). f) Xieite (Xie) occurring in the shock-melt vein. Spherical metallic iron-nickel (Fe-Ni)-iron-sulfide assemblage grains with eutectic textures occur in the matrix portion of the shock-melt vein. TEM bars in (d) and (e) are areas excavated by FIB (see Fig. 4).

akimotoite (Ohtani et al. 2004; Ozawa et al. 2009). Raman spectra of the original low-Ca pyroxene (mainly orthoenstatite) and Ca pyroxene (diopside) in the host-rock are compared in Figs. 3g and 3i, respectively. The chemical compositions of low-Ca pyroxene, diopside, majorite, and akimotoite

determined by EMPA are summarized in Table 3. The sodium and aluminum contents of akimotoite are slightly higher than those of the original low-Ca pyroxene, although there are few differences in the chemical compositions between majorite and the original low-Ca pyroxene. The fine-grained, needle-shaped

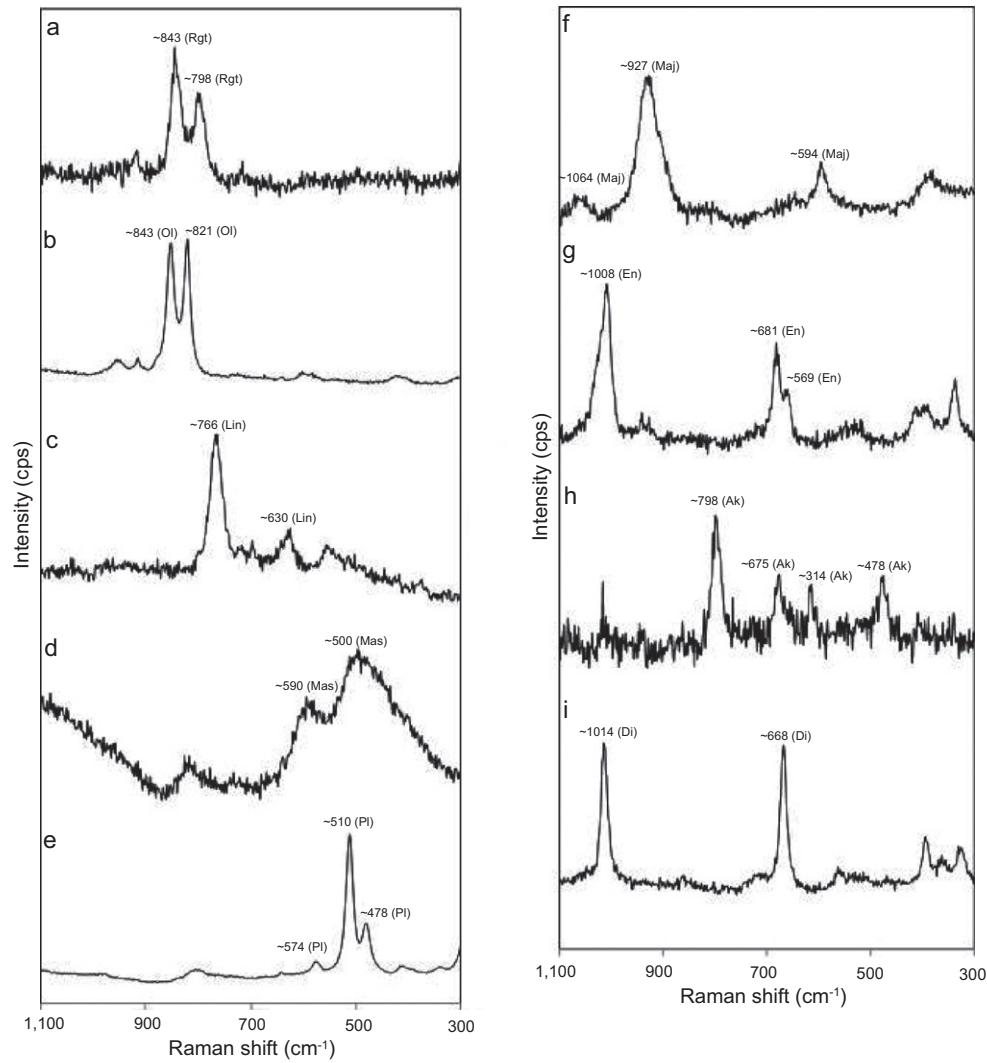


Fig. 3. Representative Raman spectra of (a) ringwoodite (Rgt), (b) olivine (Ol), (c) lingunite (Lin), (d) maskelynite (Mas), (e) plagioclase (Pl), (f) majorite (Maj), (g) orthoenstatite (En), (h) akimotoite (Ak), and (i) diopside (Di).

akimotoite polycrystalline assemblage was observed by a TEM (Figs. 2e and 4b). Although the chemical compositions of individual akimotoite grain were determined by STEM-EDS (Table 2), the sodium content in akimotoite could not be determined due to serious loss of sodium during electron beam irradiation.

High-Pressure Polymorphs of Plagioclase

Two broad Raman shifts on most plagioclase in the host-rock (Fig. 3d) appear at ~ 500 and ~ 590 cm^{-1} instead of diagnostic Raman shift for plagioclase (~ 478 and ~ 510 cm^{-1}) (Fig. 3e). They correspond to those of maskelynite (Chen and El Goresy 2000; Ohtani et al. 2004). Raman analyses indicate that most grains of

plagioclase entrained in the shock-melt vein have transformed into hollandite-type $\text{NaAlSi}_3\text{O}_8$, lingunite (Figs. 2a and 3c) (Gillet et al. 2000; Tomioka et al. 2000). EMPA analyses indicate little difference in the chemical compositions between lingunite in the shock-melt vein and maskelynite in the host-rock (Table 4). Sixteen maskelynite portions in the host-rock and around the shock-melt vein were analyzed by EMPA and CL spectroscopy (Table 5). The obtained panchromatic CL images consist of bright and dark portions (Figs. 5a and 5b). CL spectra obtained from the bright portions have mainly two ultraviolet to blue emission bands at ~ 330 nm and ~ 380 nm (Fig. 5c). Similar emission bands have been reported in the CL spectra of experimentally shocked sanidine, microcline, and albite above 30 GPa (partly at 20 GPa) and those

Table 1. Chemical compositions of olivine and ringwoodite obtained by EMPA.

No. oxides	1	2	7	10	20	14	18	27
	Ringwoodite					Olivine		
SiO ₂	38.47	38.55	38.58	38.50	38.55	38.28	38.43	38.60
TiO ₂	0.01	0.02	0.02	0.06	<0.01	<0.01	0.03	<0.01
Al ₂ O ₃	0.02	<0.01	0.02	0.01	0.02	<0.01	<0.01	<0.01
Cr ₂ O ₃	<0.01	0.03	<0.01	<0.01	0.02	0.04	<0.01	0.02
FeO	22.70	22.52	22.71	22.74	22.57	23.38	22.16	22.41
MnO	0.40	0.46	0.51	0.47	0.47	0.50	0.43	0.42
MgO	38.45	38.92	39.33	39.60	39.41	38.63	39.75	39.66
NiO	0.03	<0.01	0.03	0.02	<0.01	0.07	0.02	<0.01
CaO	0.06	0.02	0.02	<0.01	0.04	0.01	<0.01	0.03
Total (wt%)	100.13	100.51	101.21	101.40	101.08	100.90	100.81	101.13
Formula (O = 4)								
Si	1.001	0.999	0.994	0.990	0.994	0.993	0.991	0.993
Ti	0.000	0.000	0.000	0.001	0.000	0.000	0.001	0.000
Al	0.001	0.000	0.001	0.000	0.001	0.000	0.000	0.000
Cr	0.000	0.001	0.000	0.000	0.000	0.001	0.000	0.000
Fe (ii)	0.494	0.488	0.489	0.489	0.487	0.507	0.478	0.482
Mn	0.009	0.010	0.011	0.010	0.010	0.011	0.009	0.009
Mg	1.492	1.503	1.510	1.518	1.514	1.494	1.528	1.521
Ni	0.001	0.000	0.001	0.000	0.000	0.001	0.000	0.000
Ca	0.002	0.000	0.000	0.000	0.001	0.000	0.000	0.001
Total	3.000	3.001	3.006	3.009	3.007	3.007	3.008	3.007
Fa (mol%)	24.8	24.4	24.3	24.2	24.2	25.2	23.7	24.0

All iron is assumed ferrous.

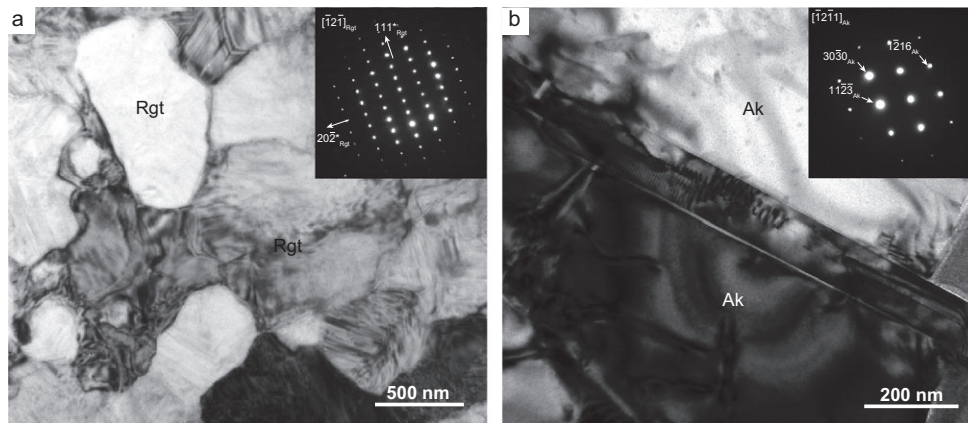


Fig. 4. Bright-field TEM images of (a) ringwoodite (Rgt) (TEM_1 in Fig. 2d) and its electron diffraction pattern at the top-right inset, and (b) akimotoite (Ak) (TEM_2 in Fig. 2e) and its electron diffraction pattern at the top-right inset.

of maskelynite in Martian meteorites (Kayama et al. 2012). Such a spectral pattern is characteristic of maskelynite and diaplectic feldspar glass, and undetectable in crystalline plagioclase (Kayama et al. 2009a, 2009b, 2012). On the other hand, the CL spectroscopy of the dark portion exhibits only a blue emission band at ~ 410 nm (Fig. 5c). Crystalline plagioclase in rocks also shows the blue emission bands (Kayama et al. 2009a, 2009b, 2012). Therefore, the bright and dark portions observed in the panchromatic

CL images correspond to maskelynite and residual plagioclase, respectively.

Other High-Pressure Polymorphs

Detailed Raman spectroscopy revealed the presence of several minor minerals, such as apatite, tuite, chromite, and xieite in Y-790729. Several apatite grains (diameter $< \sim 50$ μm) were entrained in the shock-melt vein. Diagnostic Raman spectrum of apatite (P-O stretching)

Table 2. Chemical compositions of akimotoite and ringwoodite obtained by STEM-EDS.

No. oxides	V_04_58	V_04_66	V_04_71	V_04_74	V_04_72	V_05_4	V_05_30	V_05_31	V_05_26	V_05_28
	Akimotoite					Ringwoodite				
SiO ₂	57.3	56.4	56.0	56.0	55.7	38.9	38.9	38.1	37.9	38.0
Al ₂ O ₃	<0.1	<0.1	1.0	0.1	0.4	–	–	–	–	–
MgO	31.3	29.9	30.8	30.1	30.3	38.7	38.9	38.5	38.4	39.1
FeO	11.1	13.7	12.2	13.8	13.4	22.5	22.2	23.4	23.7	22.9
CaO	0.3	<0.1	<0.1	<0.1	0.3	–	–	–	–	–
Total (wt%)	100	100	100	100	100	100	100	100	100	100
Formula										
O =	6	6	6	6	6	4	4	4	4	4
Si	4.02	4.01	3.96	3.99	3.96	1.01	1.01	1.00	0.99	0.99
Al	0.00	0.00	0.08	0.01	0.03	–	–	–	–	–
Mg	3.28	3.17	3.24	3.19	3.21	1.49	1.50	1.50	1.50	1.52
Fe (ii)	0.65	0.81	0.72	0.82	0.80	0.49	0.48	0.51	0.52	0.50
Ca	0.02	0.00	0.00	0.00	0.02	–	–	–	–	–
Total	7.98	7.99	8.00	8.01	8.02	2.99	2.99	3.00	3.01	3.01
Fa (mol%)	–	–	–	–	–	24.6	24.2	25.5	25.7	24.7

All iron is assumed ferrous. Total is normalized to 100%. – = not determined.

Table 3. Chemical compositions of pyroxene, majorite, and akimotoite obtained by EMPA.

No. oxides	3	8	11	15	16	23	26	28	5	17	108	24	25
	Low-Ca pyroxene								Ca pyroxene		Majorite	Akimotoite	
SiO ₂	54.99	55.48	55.90	55.45	55.16	55.54	55.11	54.65	53.95	53.55	54.91	55.84	55.79
TiO ₂	0.24	0.19	0.15	0.15	0.17	0.18	0.15	0.19	0.51	0.46	0.21	0.19	0.08
Al ₂ O ₃	0.19	0.14	0.13	0.13	0.13	0.19	0.16	0.15	0.50	0.49	0.16	0.23	0.63
Cr ₂ O ₃	0.13	0.19	0.13	0.13	0.11	0.15	0.08	0.13	0.87	0.91	0.09	0.14	0.19
FeO	13.80	13.52	13.59	13.56	13.62	13.10	13.74	13.95	4.85	4.99	14.09	14.39	11.80
MnO	0.48	0.48	0.43	0.50	0.48	0.52	0.47	0.49	0.25	0.25	0.54	0.54	0.36
MgO	29.20	29.20	29.22	29.10	28.69	29.23	29.52	28.91	16.72	16.73	28.73	28.47	31.01
CaO	0.82	0.81	0.74	0.87	0.85	0.84	0.64	0.94	22.28	21.59	0.68	0.89	0.69
Na ₂ O	0.03	0.03	0.05	0.01	0.03	0.02	0.01	0.01	0.63	0.57	<0.01	0.22	0.33
K ₂ O	<0.01	<0.01	<0.01	0.01	<0.01	<0.01	<0.01	0.01	<0.01	<0.01	<0.01	0.02	0.03
Total (wt%)	99.89	100.04	100.34	99.92	99.24	99.76	99.87	99.43	100.56	99.54	99.39	100.91	100.90
Formula (O = 6)													
Si	1.973	1.983	1.990	1.985	1.988	1.986	1.975	1.973	1.971	1.974	1.981	1.987	1.963
Ti	0.007	0.005	0.004	0.004	0.005	0.005	0.004	0.005	0.014	0.013	0.006	0.005	0.002
Al	0.008	0.006	0.006	0.006	0.005	0.008	0.007	0.006	0.022	0.021	0.007	0.009	0.026
Cr	0.004	0.005	0.004	0.004	0.003	0.004	0.002	0.004	0.025	0.027	0.003	0.004	0.005
Fe (ii)	0.414	0.404	0.405	0.406	0.411	0.392	0.412	0.421	0.148	0.154	0.425	0.428	0.347
Mn	0.015	0.014	0.013	0.015	0.015	0.016	0.014	0.015	0.008	0.008	0.016	0.016	0.011
Mg	1.562	1.556	1.551	1.553	1.542	1.559	1.577	1.556	0.910	0.920	1.545	1.510	1.627
Ca	0.031	0.031	0.028	0.033	0.033	0.032	0.024	0.036	0.872	0.853	0.026	0.034	0.026
Na	0.002	0.002	0.003	0.001	0.002	0.001	0.001	0.001	0.045	0.041	0.000	0.015	0.022
K	0.000	0.000	0.000	0.001	0.000	0.000	0.000	0.000	0.000	0.000	0.000	0.001	0.001
Total	4.016	4.007	4.003	4.007	4.004	4.003	4.017	4.018	4.014	4.010	4.009	4.009	4.031
Fs	21.1	20.8	20.9	20.9	21.2	20.4	20.9	21.4	7.8	8.2	21.9	22.1	17.5
En	77.2	77.5	77.6	77.4	77.0	78.0	77.8	76.8	45.9	46.6	76.8	75.4	80.1
Wo	1.6	1.5	1.4	1.7	1.6	1.6	1.2	1.8	44.0	43.2	1.3	1.7	1.3

All iron is assumed ferrous.

Table 4. Chemical compositions of lingunite and maskelynite obtained by EMPA.

No. oxides	89	90	91	92	93	94	95	96
	Lingunite		Maskelynite					
SiO ₂	65.49	65.03	65.18	65.41	65.10	65.59	65.59	64.87
Al ₂ O ₃	21.22	21.03	21.49	21.34	21.86	21.65	21.84	21.18
FeO	0.34	0.38	0.24	0.30	0.25	0.32	0.35	0.17
CaO	2.14	2.13	1.94	2.05	2.17	2.18	2.10	2.12
Na ₂ O	9.94	9.92	9.92	9.72	9.62	9.78	9.80	9.88
K ₂ O	1.05	0.85	1.00	1.06	0.81	1.05	0.94	0.96
Total (wt%)	100.18	99.34	99.76	99.88	99.80	100.57	100.62	99.18
Formula (O = 32)								
Si	11.554	11.561	11.532	11.559	11.495	11.519	11.506	11.546
Al	4.412	4.407	4.480	4.444	4.550	4.481	4.514	4.443
Fe (ii)	0.051	0.056	0.035	0.045	0.037	0.047	0.051	0.025
Ca	0.405	0.405	0.368	0.388	0.411	0.411	0.394	0.404
Na	3.400	3.417	3.402	3.329	3.293	3.331	3.334	3.410
K	0.235	0.193	0.226	0.240	0.182	0.235	0.211	0.218
Total	20.057	20.041	20.042	20.004	19.967	20.023	20.010	20.046
An	10.0	10.1	9.2	9.8	10.6	10.3	10.0	10.0
Ab	84.1	85.1	85.2	84.1	84.8	83.8	84.6	84.6
Or	5.8	4.8	5.6	6.1	4.7	5.9	5.4	5.4

All iron is assumed ferrous.

Table 5. Details of CL spectra of maskelynite.

No.	D (mm)	Intensities			Chemical compositions obtained by EMPA						Shock <i>P</i>
		2.95 eV	3.26 eV	3.88 eV	SiO ₂	Al ₂ O ₃	Na ₂ O	CaO	K ₂ O	Total (wt%)	
01_A_1	0.82	390.2	1977.4	1120.5	65.90	21.81	8.99	2.22	1.08	100.00	13.7
01_B_1	0.36	556.0	1760.6	1439.9	65.58	21.60	9.32	2.16	1.01	99.67	16.7
02_1	0.01	625.6	2207.7	1520.8	65.25	21.29	9.70	2.17	1.03	99.44	18.0
02_2	0.01	697.9	1985.4	1444.5	65.00	21.25	9.39	2.10	1.62	99.37	19.3
03_A_1	1.01	669.1	1810.5	1814.6	66.07	22.03	8.95	2.14	1.18	100.37	18.8
03_B_1	1.58	678.1	1791.3	1662.9	65.34	21.21	9.65	2.23	0.89	99.31	19.0
07_3	4.94	242.2	2142.1	897.7	65.83	21.69	9.54	2.19	1.17	100.43	10.9
07_B_1	4.59	466.9	1281.8	1353.3	65.46	20.99	9.55	2.07	1.06	99.12	15.1
13_1	2.05	546.1	1191.9	1018.4	64.39	21.05	9.68	2.23	0.96	98.32	16.5
13_3	2.87	240.7	972.5	2145.0	66.53	21.87	8.48	2.23	0.98	100.09	10.9
14_1	1.58	508.9	1567.6	2216.7	65.39	21.45	9.97	2.15	0.95	99.91	15.8
14_2	1.27	590.1	942.6	1363.3	64.88	21.60	9.92	2.08	0.89	99.37	17.3
20_1	0.03	430.1	1482.8	1970.6	65.38	21.71	9.81	2.14	0.93	99.96	14.4
20_2	0.03	472.1	1662.7	2024.0	65.55	21.38	8.93	2.22	1.39	99.47	15.2
22_1	0.06	343.6	1639.1	2297.7	66.01	21.95	8.10	2.20	0.98	99.24	12.8
22_2	0.14	427.7	1638.8	2512.5	66.69	21.92	9.29	2.15	1.01	101.06	14.3

D = distance from a shock-melt vein. *P* = estimated pressure (GPa).

appears at ~ 962 cm⁻¹ (Figs. 6a and 6b) (Wopenka and Pasteris 2005). Another Raman spectrum appears at ~ 979 cm⁻¹ from some apatite grains (Figs. 2c and 6a), indicating that they have been partly transformed into the high-pressure polymorph of apatite, tuite (Xie et al. 2002, 2003). Several grains of aluminum-bearing chromite (diameter $< \sim 50$ μ m) were also entrained in the shock-melt vein. Diagnostic Raman spectrum of chromite (A_{1g} mode

generated by the bonds in [Cr³⁺, Fe³⁺, Al³⁺] O₆ octahedra) appeared at ~ 682 cm⁻¹ (Fig. 6d) (Wang et al. 2004; Stanojević et al. 2007). A broad Raman shift at ~ 607 cm⁻¹ with a shoulder around ~ 665 cm⁻¹ appeared from some grains having chromite composition (Figs. 2f and 6c; Table 6), which coincides with that of the orthorhombic CaTi₂O₄-structured chromite, xieite (Chen et al. 2003a, 2003b, 2008; Xie et al. 2011).

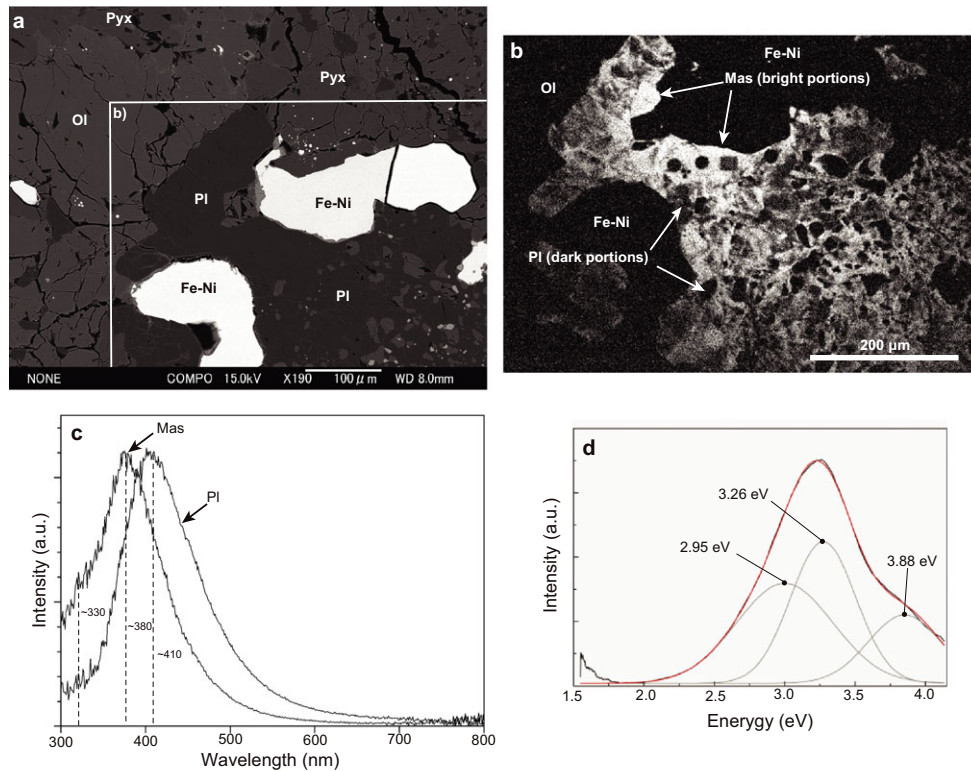


Fig. 5. Representative cathodoluminescence (CL) spectra. a) BSE image of plagioclase (now maskelynite) in the host-rock. b) The panchromatic CL image of the square in (a). Brightness contrast corresponds to the change of bright maskelynite to dark plagioclase. c) A comparison of CL spectra between maskelynite and crystalline plagioclase. d) The deconvoluted CL spectrum of maskelynite. Ol = olivine; Pyx = low-Ca pyroxene; Pl = plagioclase; Fe-Ni = iron-nickel alloy.

DISCUSSION

Shock Pressure Estimation Based on High-Pressure Polymorphs

Ringwoodite, majorite, akimotoite, tuite, and xieite were identified as high-pressure polymorphs in and around the shock-melt veins of Y-790729 L6 studied here. The inventory of high-pressure polymorphs in Y-790729 is similar to that in other L6 ordinary chondrites (Chen et al. 1996; Ohtani et al. 2004; Xie et al. 2006; Miyahara et al. 2015). Assuming that these high-pressure polymorphs were formed under the equilibrated condition during an impact event because mineral species, their assemblages, chemical compositions, and grain sizes in the shock-melt veins of ordinary chondrites are akin to those in synthetic samples recovered from high-pressure and -temperature melting experiments using Allende and peridotite, pressure and temperature conditions could be estimated by the coexistence conditions of the high-pressure polymorph assemblages (Chen et al. 1996; Ohtani et al. 2004; Xie et al. 2006; Miyahara et al. 2008; Ozawa

et al. 2009). Original olivine ($\text{Mg}_{1.515}\text{Fe}_{0.489}\text{Si}_{0.993}\text{O}_4$, $\text{Fa}_{24.3}$ on average) in and around the shock-melt veins of Y-790729 has transformed into ringwoodite ($\text{Mg}_{1.508}\text{Fe}_{0.489}\text{Si}_{0.995}\text{O}_4$, $\text{Fa}_{24.4}$ on average) (Figs. 2a and 2b; Tables 1 and 2). The ringwoodite does not accompany wadsleyite (e.g., Miyahara et al. 2008), or wadsleyite does occur as a replacement of olivine (e.g., Ozawa et al. 2009). Based on the phase diagram in the Mg_2SiO_4 - Fe_2SiO_4 system (Ohtani 1979; Presnall 1995) and the high-pressure melting experiment of Allende CV3 carbonaceous chondrite (Agee et al. 1995), the minimum pressure required for the phase transformation from olivine to ringwoodite is ~ 14 GPa. The dissociation reaction from olivine to bridgmanite + magnesiowüstite (e.g., Miyahara et al. 2011) was not observed in Y-790729, implying shock pressures close to or below ~ 23 GPa. Little difference in the chemical compositions between the original olivine and ringwoodite (Tables 1 and 2) suggests that the phase transition from olivine to ringwoodite occurs without the Fe-Mg interdiffusion. TEM observations reveal that ringwoodite in the shock-melt veins is a polycrystalline assemblage (Fig. 4a). These features have

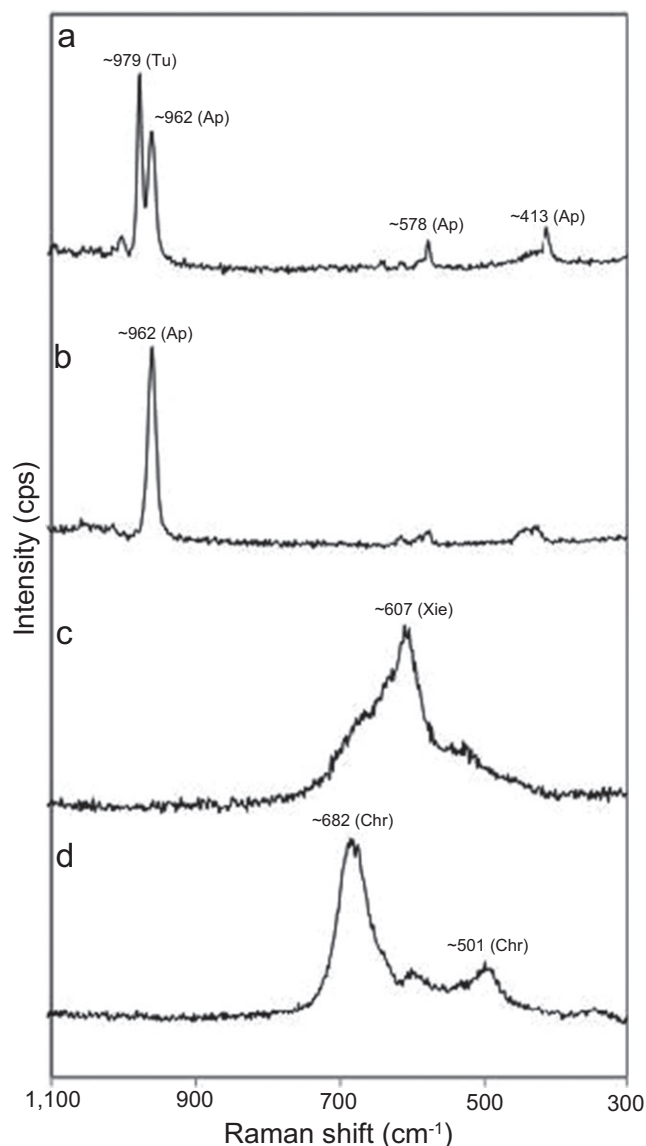


Fig. 6. Representative Raman spectra of (a) apatite (Ap) with tutite (Tu), (b) Ap, (c) xieite (Xie), and (d) chromite (Chr).

been observed in ringwoodite of many heavily shocked ordinary chondrites (Chen et al. 2007; Miyahara et al. 2010), and indicate that the phase transition from olivine to ringwoodite in Y-790729 is controlled by interface-controlled nucleation and grain-growth mechanism.

Original low-Ca pyroxene ($\text{Ca}_{0.031}\text{Na}_{0.002}\text{Mg}_{1.557}\text{Fe}_{0.408}\text{Mn}_{0.015}\text{Cr}_{0.004}\text{Ti}_{0.005}\text{Al}_{0.006}\text{Si}_{1.982}\text{O}_6$, $\text{Fs}_{21.0}\text{En}_{77.4}\text{Wo}_{1.6}$ on average) (Table 3) entrained in the shock-melt veins has transformed into majorite and akimotoite (Figs. 2d and 2e). The phase diagram of MgSiO_3 at high pressure indicates that majorite and akimotoite appear at high and low temperatures under almost the

Table 6. Chemical compositions of chromite and xieite obtained by EMPA.

	13	6
No. oxides	Chromite	Xieite
SiO_2	<0.01	0.10
TiO_2	3.12	3.00
Al_2O_3	5.86	5.73
Cr_2O_3	56.57	56.65
FeO	30.10	30.21
MnO	0.71	0.71
MgO	2.77	2.92
CaO	0.01	0.03
Total (wt%)	99.13	99.34
Formula (O = 32)		
Si	0.000	0.028
Ti	0.670	0.643
Al	1.972	1.923
Cr	12.773	12.767
Fe (ii)	7.190	7.202
Mn	0.171	0.172
Mg	1.180	1.239
Ca	0.002	0.008
Total	23.958	23.983

All iron is assumed ferrous.

same pressure condition, respectively (Gasparik 1990; Hirose et al. 2001). Poorly crystallized or amorphous material with a chemical composition of low-Ca pyroxene, which is observed in some heavily shocked L6 ordinary chondrites (e.g., Miyahara et al. 2010), was not identified in the shock-melt veins of Y-790729. The poorly crystallized or amorphous material with a chemical composition of low-Ca pyroxene is regarded as vitrified bridgmanite (Tomioka and Fujino 1997). Considering the coexistence of majorite and akimotoite and the absence of bridgmanite, the shock pressure and temperature conditions can be estimated to be ~16–25 GPa and ~873–2873 K, respectively. Several diopside grains ($\text{Ca}_{0.862}\text{Na}_{0.043}\text{Mg}_{0.915}\text{Fe}_{0.151}\text{Mn}_{0.015}\text{Cr}_{0.008}\text{Ti}_{0.013}\text{Al}_{0.021}\text{Si}_{1.973}\text{O}_6$, $\text{Fs}_{8.0}\text{En}_{46.3}\text{Wo}_{43.6}$ on average) are entrained in the shock-melt veins of Y-790729 (Table 3). The phase diagram of diopside at high pressure indicates that diopside dissociates into CaSiO_3 with a perovskite structure + majorite or akimotoite at pressures of 17–18 GPa and temperatures of 1373–2373 K (Canil 1994). However, the intact diopside grains entrained in the shock-melt veins suggest a shock pressure of less than ~18 GPa.

Apatite entrained in the shock-melt veins has transformed into tutite (Figs. 2c and 6a). Although the phase relation between apatite and tutite has not been determined in detail, the existence of tutite might indicate shock pressures beyond ~10 GPa (Murayama

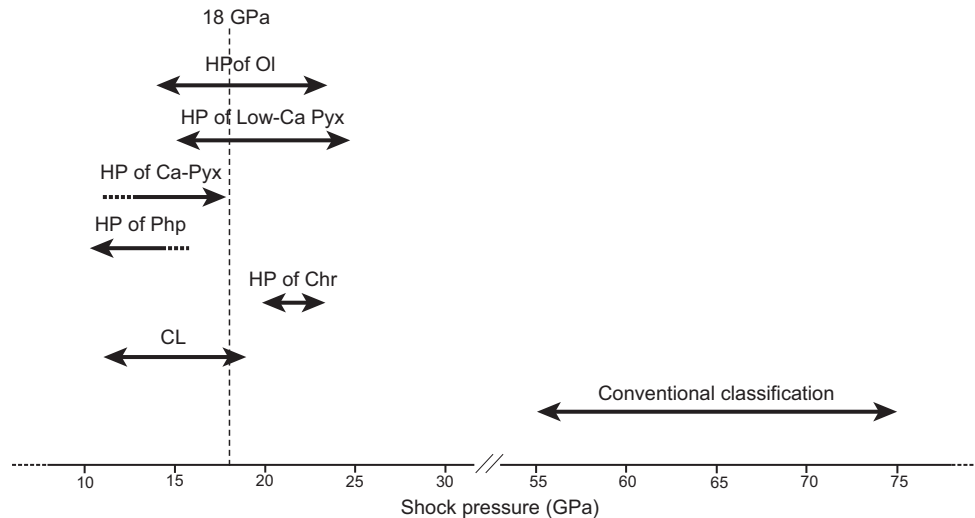


Fig. 7. A comparison of shock pressures estimated by high-pressure polymorphs of olivine (Ol), pyroxene (Pyx), phosphate (Php), and chromite (Chr) observed in the present study, calibrated CL barometer of maskelynite, and conventional classification proposed by Stöffler et al. (1991).

et al. 1986). Chromite entrained in the shock-melt vein has transformed into xieite (Figs. 2f and 6c–d), implying shock pressures of ~20 to ~23 GPa (Chen et al. 2003a, 2003b).

Based on the stability fields of the high-pressure polymorph assemblages observed in the shock-melt veins of Y-790729, the shock pressures could be estimated to be around 14–23 GPa (Fig. 7), although there is no consistent pressure based on the coexistence of all the observed high-pressure polymorphs. The rims of olivine, pyroxene, and plagioclase fragments entrained in the shock-melt vein show evidence for melting because their outlines are rounded (Figs. 2a and 2c). Fine-grained dendritic crystals and spherical metallic iron-nickel-iron-sulfide assemblage grains with eutectic textures occur in the matrices of the shock-melt veins. These features indicate that Y-790729 was heated along the shock-melt veins to a temperature beyond its liquidus. Considering the high-pressure melting experiment of Allende CV3 carbonaceous chondrite (Agee et al. 1995), the shock-melt veins would be heated up to a temperature of about 2173–2573 K. The high-pressure polymorphs applied for shock pressure estimation were formed through solid-state transformation. Xie et al. (2006) proposed that a high-pressure polymorph crystallized from melts in a shock-melt vein records more accurate pressure condition compared to the pressure condition deduced from a high-pressure polymorph formed in chondritic or mineral fragments entrained in the shock-melt vein. However, significant difference would not be expected (Ohtani et al. 2004; Hu and Sharp 2016; Walton and McCarthy 2017).

Shock Pressure Estimation Based on CL Spectra

Deconvolution of the CL spectra in energy unit scale successfully separates the ultraviolet to blue emission bands of maskelynite into three Gaussian components centered at 2.95, 3.26, and 3.88 eV. The number, peak position, and full width at half maximum of these Gaussian components can be determined by the procedure and reference values reported in Kayama et al. (2010, 2012). As the components at 3.26 and 3.88 eV are detectable only in the CL spectra of maskelynite and experimentally shock-induced feldspar glasses (Kayama et al. 2012), they are characteristic of various defect centers in amorphous feldspar. The component at 2.95 eV is observed in not only shocked crystalline feldspar but also in the diaplectic glass and meteoritic maskelynite, and identified as a luminescent property of the shock-induced defect center (Kayama et al. 2012). However, overlapping of the component at 2.95, 3.26, and 3.88 eV with other components assigned to the UV-blue luminescent centers (e.g., Ce^{3+} , Eu^{2+} , Ti^{4+} , and Al-O^- -Al/Ti defect) seems to make it difficult to deconvolute each other from CL spectra of plagioclase because of the following reason. In the case of plagioclase, many and various types of intrinsic emission components, e.g., Ce^{3+} at 3.9 eV, Eu^{2+} at 3.0 eV, Ti^{4+} at 3.055–3.076 eV, and Al-O^- -Al/Ti defect at 2.815–2.845 eV, are broader in width, and are centered in the narrow range from the UV-blue regions, beside the shock-induced components at 2.95, 3.26, and 3.88 eV (Götze et al. 2001; Kayama et al. 2009a, 2012). On the other hand, these intrinsic emission components act as a luminescent center of only crystalline

plagioclase, but not the amorphous one, implying simpler deconvolution procedures for three shock-induced components of maskelynite. Therefore, we applied integral intensities of the components at 2.95, 3.26, and 3.88 eV for the maskelynite to deduce the shock pressure that Y-790729 has experienced.

According to a previous CL study (Kayama et al. 2012), the integral intensities of the emission components at 2.95, 3.26, and 3.88 eV increase with shock pressure. However, the intensities of the components at 3.26 and 3.88 eV depend on not only the shock pressure but also many factors including the chemical compositions between Na and K contents, structural ordering, phase transition, crystallinity, and probably posttemperature. On the other hand, the component at 2.95 eV appears to change little in the intensity with these factors, compared with the other components (Kayama et al. 2012). CL spectral data of 16 portions of maskelynite were deconvolved in order to estimate the shock pressure on Y-790729. They show only three emission components centered at 2.96, 3.26, and 3.88 eV (Figs. 5c and 5d). Actually, the standard deviations of the integral intensities at 3.26 and 3.88 eV obtained from maskelynite in Y-790729 are much larger than those at 2.95 eV, as in the case of experimentally shocked feldspar (Kayama et al. 2012). This fact also implies that the intensities at 3.26 and 3.88 eV appear to be easily affected by such mineralogical features of the precursor of maskelynite in Y-790729, as reported previously (Jaret et al. 2015). Therefore, the intensity of the emission component at 2.95 eV is more useful for the shock estimation than those at 3.26 and 3.88 eV.

The integral intensities of the component at 2.95 eV are plotted against six major oxides in maskelynite of Y-790729 (Fig. 8). All the contents of major oxides have almost no correlation with the emission intensity at 2.95 eV (Fig. 8). Therefore, the shock pressure that Y-790729 has experienced can be inferred without calibration to the major elemental contents of each maskelynite. Based on the intensity at 2.95 eV and the shock barometer obtained from experimental samples (Kayama et al. 2012), we estimated shock pressures of 11–19 GPa from maskelynite in Y-790729 (Table 5).

A Comparison of Shock Conditions Among Three Different Methods

The shock pressure conditions estimated by (1) high-pressure polymorph assemblages, (2) CL spectrum, and (3) conventional shock metamorphism classification are summarized in Fig. 7. Methods (1) and (2) indicate similar results to each other. Method (3) is based on macroscopic comparisons between natural shocked

ordinary chondrites and experimentally shocked ordinary chondrites (Stöffler et al. 1991). Following method (3), the coexistence of maskelynite, shock-melt vein, and ringwoodite gives shock pressures of ~55 to ~75 GPa (Fig. 8), which is considerably higher than those by methods (1) and (2). The shock pressures deduced from individual high-pressure polymorph species found in the shock-melt vein are 14–23 GPa (Fig. 7). This result may demonstrate that the shock pressure is heterogeneous in Y-790729. Recent simulation results on primordial (porous) chondrites (like type 3 chondrites) suggest significant heterogeneity in pressure and temperature (Bland et al. 2014), because they have large variation in shock impedance. However, Y-790729 studied here is a member of type 6, which has a low porosity and equilibrium texture. An equilibrium shock pressure estimation pinpointed from the individual phases cannot be determined in principle using method (1) because the individual mineral has a broad equilibrium pressure and temperature field. In addition, phase transition (nucleation and subsequent grain-growth) is controlled by kinetics. Even if the chondritic melt acts as a perfect pressure medium, temperature distribution and thermal history would be heterogeneous, thus leading to complicated phase assemblages affected by the transition kinetics of individual high-pressure minerals.

The shock pressure condition based on the CL spectrum also varied from 11 to 19 GPa. The panchromatic CL image depicts that the maskelynitization of original plagioclase is not homogeneous (Fig. 5b). We tried to collect CL spectra for estimating the shock pressure condition only from maskelynite portions based on the panchromatic CL image. However, we cannot rule out the possibility that the CL spectra of remnant plagioclase portions were superimposed on those of maskelynite, in part, because complete maskelynitization was not confirmed in each CL measurement.

The shock pressure condition estimated by method (1) appears to be higher than that by method (2). The shock pressure condition estimated by methods (1) and (2) comes from high-pressure polymorphs formed in the shock-melt vein and maskelynite in the host-rock, respectively. It is likely that the shock pressure conditions estimated by methods (1) and (2) correspond to those in the shock-melt vein and the host-rock, respectively. In other words, the shock condition in shock-melt vein and in host-rock may differ. If it is true, the difference may be explained as the local porosity distributions in the body before the impact event, although the body has been impact-sintered considerably. The stability field of a high-pressure phase was determined experimentally as an endmember mineral in most cases. On the other hand, most

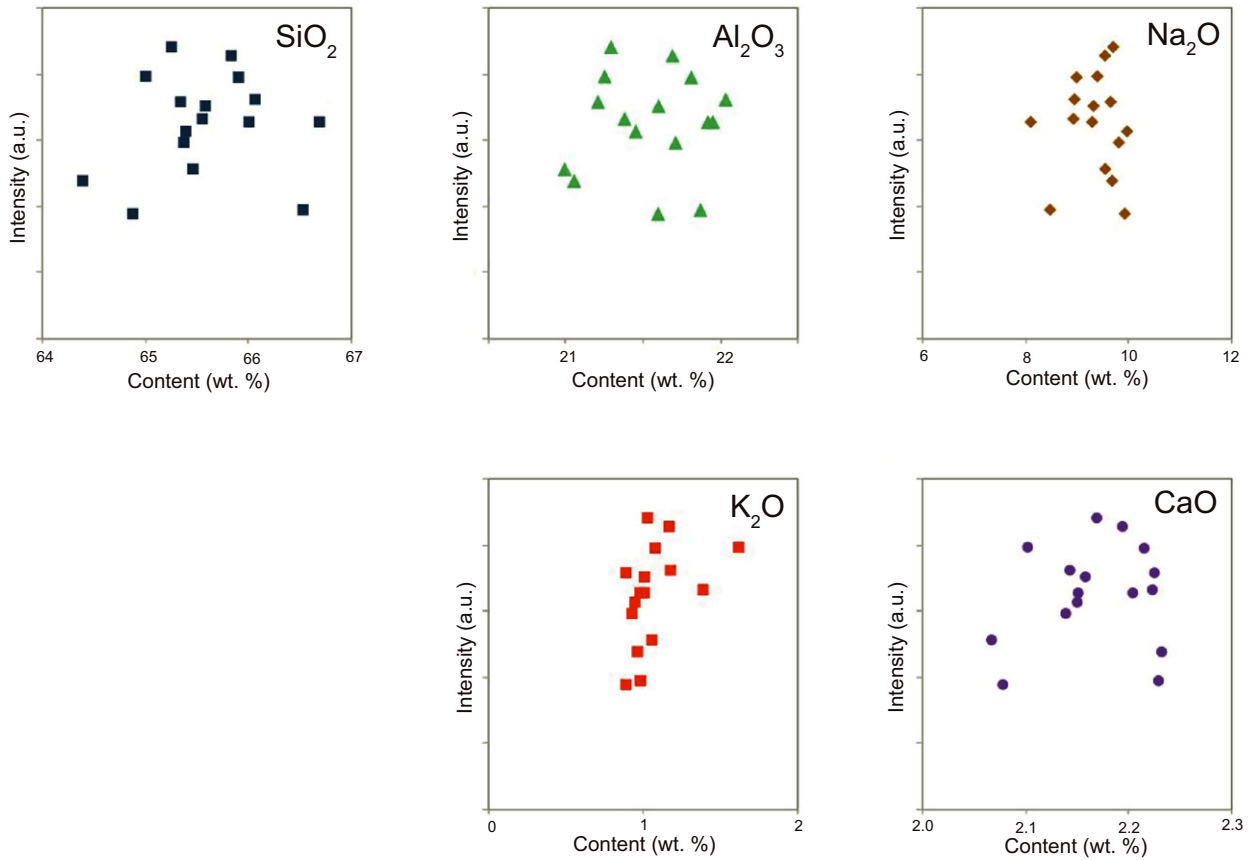


Fig. 8. Relationships between the intensities at 2.95 eV peak and chemical compositions of major oxides in plagioclase (now maskelynite).

constituents in Y-790729 are not endmember minerals. The stability field of a high-pressure phase also depends on the chemical composition of an individual mineral besides pressure and temperature conditions. It is possible that the estimated shock pressure based on the stability field of a high-pressure phase might be a bit shifted.

Shock Event Magnitude Estimation

Mass, momentum, and energy are conserved across a shock front as known from the Rankine–Hugoniot equation. The shock pressure (P) can be expressed by the following equation (Ahrens and Johnson 1995).

$$P - P_0 = \rho_0 U_s U_p \quad (1)$$

where P_0 and ρ_0 are the initial pressure and density before an impact and U_s and U_p are shock wave velocity and particle velocity, respectively. In general, P_0

is negligible because it is much smaller than P . Accordingly, Equation 1 can be simplified as follows.

$$P = \rho_0 U_s U_p \quad (2)$$

The relationship between U_s and U_p is known to be linear.

$$U_s = C + S U_p \quad (3)$$

where C and S are constants depending on the material. Assuming that both projectile and target consist of the same material,

$$U_p = U_i/2 \quad (4)$$

where U_i is the head-on impact velocity. Giving $P = 18$ GPa in Y-790729 and assuming an ordinary chondrite with $\rho_0 = 3.44$ g cm⁻³, $C = 3.98$, and $S = 1.37$ (Zhang and Sekine 2007), the calculated U_p , U_s , and U_i are 1.00 km s⁻¹, 5.26 km s⁻¹, and

1.99 km s⁻¹, respectively. The head-on impact velocity estimated for Y-790729 is within the range of the computed impact velocity distribution in the Main Belt (Bottke et al. 1994).

Grain-growth subsequent to nucleation is kinetically controlled. Ohtani et al. (2004) measured the grain size of ringwoodite and estimated the duration of high-pressure and -temperature conditions required for the growth of ringwoodite by integrating the kinetic parameters of ringwoodite and temperature history. Ringwoodite occurring in the shock-melt veins of Y-790729 has a radius of about 50 μm under an optical microscope. However, TEM observations indicate that ringwoodite is a polycrystalline assemblage (Fig. 4a). Individual ringwoodite grain is from ~0.1 to ~1.3 μm across. Phase transformation from olivine to ringwoodite is controlled mainly by coherent and incoherent mechanisms (Boland and Liu 1983; Remsberg et al. 1988; Burnley and Green 1989; Kerschhofer et al. 1996, 1998; Mosenfelder et al. 2001). There is a distinct difference in their growth rates between coherent and incoherent phase transition mechanisms (Liu et al. 1998; Kerschhofer et al. 2000). The ringwoodite in the shock-melt veins of Y-790729 is granular and polycrystalline, being suggestive of incoherent phase transformation. Most previous studies also support that the dominant phase transition mechanism from olivine to ringwoodite is an incoherent process (Ohtani et al. 2004; Chen et al. 2007; Miyahara et al. 2010). The chondritic fragment entrained in the shock-melt vein of Y-790729 includes the olivine grain replaced with polycrystalline ringwoodite. The chondritic fragment is about 300 × 100 μm, which is large compared to surrounding shock-melt veins. Accordingly, we used the simplified one-dimensional model used in Ohtani et al. (2004). The distance from the olivine grain replaced with polycrystalline ringwoodite to the host-rock of Y-790729 is ~120 μm. TEM images show that individual ringwoodite grain is <~1.3 μm across. The melting temperature of the L6 ordinary chondrite appears to be close to those of KLB-1 peridotite and Allende CV3 (Agee et al. 1995; Herzberg and Zhang 1996; Asahara et al. 2004). The melting temperature could be about 2173 K at 18 GPa. Although the estimated melting temperature in the present case is different from that of Ohtani et al. (2004), other features are similar. Accordingly, it is likely that the duration of high-pressure and -temperature conditions recorded in the shock-melt veins of Y-790729 is a few seconds, implying that the parent-body size of Y-790729 is ~10 km in diameter at least.

CONCLUSIONS

1. Yamato-790729 L6 ordinary chondrite studied here consists of olivine, low-Ca pyroxene, plagioclase,

metallic Fe-Ni, and iron-sulfide with minor amounts of phosphate and chromite.

2. A shock-melt vein with a width of <~620 μm was observed in Y-790729. Many mineral or chondritic fragments were entrained in the shock-melt vein. Several high-pressure polymorphs occur in the mineral or chondritic fragments. Ringwoodite, majorite, akimotoite, lingunite, tuite, and xieite were identified as high-pressure polymorphs. Some plagioclase in the host-rock have transformed into maskelynite.
3. The estimated shock pressures are ~14 to ~23 GPa and ~11 to ~19 GPa based on the stability fields of the observed high-pressure polymorphs in the shock-melt vein and the calibrated CL spectra of maskelynite in the host-rock, respectively. They might suggest heterogeneous shock conditions in Y-790729.
4. Taking the average shock pressure of 18 GPa for Y-790729, an impact velocity of the parent-body of Y-790729 is calculated to be ~1.90 km s⁻¹ for the head-on symmetrical impact. The parent-body of Y-790729 would be at least ~10 km in size based on the incoherent mechanism of ringwoodite observed in Y-790729.

Acknowledgments—Prof. Z. Xie and S. Jaret are acknowledged for their comments on an earlier version of this manuscript. Profs. H. Hidaka, E. Ohtani, T. Sato, Dr. M. Maeda, and Y. Shibata are acknowledged for their technical support and useful comments. We thank A.E. Christian Koeberl for his useful comments. This work was partly supported by JSPS KAKENHI Grant Number 15H05748. This study was also supported by the National Institute of Polar Research (NIPR) through General Collaboration Project no. 26–31 and KP-307.

Editorial Handling—Dr. Christian Koeberl

REFERENCES

- Agee C. B., Li J., Shannon M. C., and Circone S. 1995. Pressure-temperature phase diagram for the Allende meteorite. *Journal of Geophysical Research* 100:17,725–17,740.
- Ahrens T. J. and Johnson M. L. 1995. Shock wave data for minerals. In *Mineral physics & crystallography: A handbook of physical contents*, edited by Ahrens T. J. Washington, D.C.: AGU. pp. 143–184.
- Asahara Y., Kubo T., and Kondo T. 2004. Phase relations of a carbonaceous chondrite at lower mantle condition. *Physics of the Earth and Planetary Interiors* 143–144:421–432.
- Bland P. A., Collins G. S., Davison T. M., Abreu N. M., Ciesla F. J., Muxworthy A. R., and Moore J. 2014.

- Pressure-temperature evaluation of primordial solar system solids during impact-induced compaction. *Nature Communications* 5:5451.
- Boland J. N. and Liu L.-G. 1983. Olivine to spinel transformation in Mg_2SiO_4 via faulted structures. *Nature* 303:233–235.
- Bottke F. W., Nolan C. M., Greenberg R., and Kolvoord A. R. 1994. Velocity distributions among colliding asteroids. *Icarus* 107:255–268.
- Burnley P. C. and Green II H. W. 1989. Stress dependence of the mechanism of the olivine–spinel transformation. *Nature* 338:753–756.
- Canil D. 1994. Stability of clinopyroxene at pressure-temperature conditions of the transition region. *Physics of the Earth and Planetary Interiors* 86:25–34.
- Chen M. and El Goresy A. 2000. The nature of maskelynite in shocked meteorites: Not diaplectic glass but a glass quenched from shock-induced dense melt at high pressures. *Earth and Planetary Science Letters* 179:489–502.
- Chen M., Sharp T. G., El Goresy A., Wopenka B., and Xie X. 1996. The majorite-pyrope + magnesiowüstite assemblage: Constraints on the history of shock veins in chondrites. *Science* 271:1570–1573.
- Chen M., Shu J., Mao H.-K., Xie X., and Hemley R. J. 2003a. Natural occurrence and synthesis of two new postspinel polymorphs of chromite. *Proceedings of the National Academy of Sciences* 100:14,651–14,654.
- Chen M., Shu J., Xie X., and Mao H.-K. 2003b. Natural $CaTi_2O_4$ -structured $FeCr_2O_4$ polymorph in the Suizhou meteorite and its significance in mantle mineralogy. *Geochimica et Cosmochimica Acta* 67:3937–3942.
- Chen M., Chen J., Xie X., and Xu J. 2007. A microstructural investigation of natural lamellar ringwoodite in olivine of the shocked Sixiangkou chondrite. *Earth and Planetary Science Letters* 264:277–283.
- Chen M., Shu J., and Mao H.-K. 2008. Xieite, a new mineral of high-pressure $FeCr_2O_4$ polymorph. *Chinese Science Bulletin* 53:3341–3345.
- Ferroir T., Beck P., Moortèle B. V. D., Bohn M., Reynard B., Simionovici A., El Goresy A., and Gillet P. 2008. Akimotoite in the Tenham meteorite: Crystal chemistry and high-pressure transformation mechanisms. *Earth and Planetary Science Letters* 275:26–31.
- Gasparik T. 1990. A thermodynamic model for the enstatite-diopside join. *American Mineralogist* 75:1080–1091.
- Gillet P., Chen M., Dubrovinsky L., and El Goresy A. 2000. Natural $NaAlSi_3O_8$ -hollandite in the shocked Sixiangkou meteorite. *Science* 287:1633–1636.
- Götze J., Heimann R. B., Hildebrandt H., and Gburek U. 2001. Microstructural investigation into calcium phosphate biomaterials by spatially resolved cathodoluminescence. *Werkstofftech* 32:130–136.
- Herzberg C. and Zhang J. 1996. Melting experiments on anhydrous peridotite KLB-1: Compositions of magmas in the upper mantle and transition zone. *Journal of Geophysical Research* 101:8271–8295.
- Hirose K., Komabayashi T., and Murakami M. 2001. In situ measurements of the majorite-akimotoite-perovskite phase transition boundaries in $MgSiO_3$. *Geophysical Research Letters* 22:4351–4354.
- Hu J. and Sharp T. G. 2016. High-pressure phases in shock-induced melt of the unique highly shocked LL6 chondrite Northwest Africa 757. *Meteoritics & Planetary Sciences* 51:1353–1369.
- Jaret S. J., Woerner W. R., Phillips B. L., Ehm L., Nekvasil H., Wright S. P., and Glotch T. D. 2015. Maskelynite formation via solid-state transformation: Evidence of infrared and X-ray anisotropy. *Journal of Geophysical Research: Planets* 120:570–587.
- Kayama M., Gucsik A., Nishido H., Ninagawa K., and Tsuchiyama A. 2009a. A cathodoluminescence and Raman spectroscopic characterization of experimentally shocked plagioclase. *AIP Conference Proceedings* 1163:86–95.
- Kayama M., Nakazato T., Nishido H., Ninagawa K., and Gucsik A. 2009b. Cathodoluminescence characterization of maskelynite and alkali feldspar in Shergottite (Dhofar 019). *AIP Conference Proceedings* 1163:135–140.
- Kayama M., Nakano S., and Nishido H. 2010. Characteristics of emission centers in alkali feldspar: A new approach by using cathodoluminescence spectral deconvolution. *American Mineralogist* 95:1783–1795.
- Kayama M., Nishido H., Sekine T., Nakazato T., Gucsik A., and Ninagawa K. 2012. Shock barometer using cathodoluminescence of alkali feldspar. *Journal of Geophysical Research* 117:E09004.
- Kerschhofer L., Sharp T. G., and Rubie D. C. 1996. Intracrystalline transformation of olivine to wadsleyite and ringwoodite under subduction zone conditions. *Science* 274:79–81.
- Kerschhofer L., Dupas C., Liu M., Sharp T. G., Durham W. B., and Rubie D. C. 1998. Polymorphic transformations between olivine, wadsleyite and ringwoodite: Mechanisms of intracrystalline nucleation and the role of elastic strain. *Mineralogical Magazine* 62:617–638.
- Kerschhofer L., Rubie D. C., Sharp T. G., McConnell J. D. C., and Dupas-Bruzek C. 2000. Kinetics of intracrystalline olivine–ringwoodite transformation. *Physics of the Earth and Planetary Interiors* 121:59–76.
- Liu M., Kerschhofer L., Mosenfelder L. J., and Rubie D. C. 1998. The effect of strain energy on growth rates during the olivine–spinel transformation and implications for olivine metastability in subducting slabs. *Journal of Geophysical Research* 103:23,897–23,909.
- McMillan P., Akaogi M., Ohtani E., Williams Q., Nieman R., and Sato R. 1989. Cation disorder in garnets along the $Mg_3Al_2Si_3O_{12}$ – $Mg_4Si_4O_{12}$ join: An infrared, Raman and NMR study. *Physics and Chemistry of Minerals* 16:428–435.
- Miyahara M., El Goresy A., Ohtani E., Nagase T., Nishijima M., Vashaei Z., Ferroir T., Gillet P., Dubrovinsky L., and Simionovici A. 2008. Evidence for fractional crystallization of wadsleyite and ringwoodite from olivine melts in chondrules entrained in shock-melt veins. *Proceedings of the National Academy of Sciences* 105:8542–8547.
- Miyahara M., Ohtani E., Kimura M., El Goresy A., Ozawa S., Nagase T., Nishijima M., and Hiraga K. 2010. Coherent and subsequent incoherent ringwoodite growth in olivine of shocked L6 chondrites. *Earth and Planetary Science Letters* 295:321–327.
- Miyahara M., Ohtani E., Ozawa S., Kimura M., El Goresy A., Sakai T., Nagase T., Hiraga K., Hirao N., and Ohishi Y. 2011. Natural dissociation of olivine to $(Mg,Fe)SiO_3$ perovskite and magnesiowüstite in a shocked Martian meteorite. *Proceedings of the National Academy of Sciences* 108:5999–6003.

- Miyahara M., Ozawa S., Ohtani E., Kimura M., Kubo T., Sakai T., Nagase T., Nishijima M., and Hirao N. 2013. Jadeite formation in shocked ordinary chondrites. *Earth and Planetary Science Letters* 373:102–108.
- Miyahara M., Yamaguchi A., Ohtani E., and Saitoh M. 2015. The systematic investigations of high-pressure polymorphs in shocked L type ordinary chondrites. The Sixth Symposium on Polar Science OA_00049.
- Mosenfelder J. L., Marton F. C., Ross II C. R., Kerschhofer L., and Rubie D. C. 2001. Experimental constraints on the depth of olivine metastability in subducting lithosphere. *Physics of the Earth and Planetary Interiors* 127:165–180.
- Murayama J. K., Nakai S., Kato M., and Kumazawa M. 1986. A dense polymorph of $\text{Ca}_3(\text{PO}_4)_2$: A high pressure phase of apatite decomposition and its geochemical significance. *Physics of the Earth and Planetary Interiors* 44:293–303.
- Nakamura T., Noguchi T., Tanaka M., Zolensky M. E., Kimura M., Tsuchiyama A., Nakato A., Ogami T., Ishida H., Uesugi M., Yada T., Shirai K., Fujimura A., Okazaki R., Sandford S. A., Ishibashi Y., Abe M., Okada T., Ueno M., Mukai T., Yoshikawa M., and Kawaguchi J. 2011. Itokawa dust particles: A direct link between S-type asteroids and ordinary chondrites. *Science* 333:1113–1116.
- Ohtani E. 1979. Melting relation of FeSiO_4 up to about 200 kbar. *Journal of Physics of the Earth* 27:189–208.
- Ohtani E., Kimura Y., Kimura M., Takata T., Kondo T., and Kubo T. 2004. Formation of high-pressure minerals in shocked L6 chondrite Yamato 791384: Constraints on shock conditions and parent body size. *Earth and Planetary Science Letters* 227:505–515.
- Ozawa S., Ohtani E., Miyahara M., Suzuki A., Kimura M., and Ito Y. 2009. Transformation textures, mechanisms of formation of high-pressure minerals in shock melt veins of L6 chondrites, and pressure-temperature conditions of the shock events. *Meteoritics & Planetary Science* 44:1771–1786.
- Ozawa S., Miyahara M., Ohtani E., Koroleva O. N., Ito Y., Litasov K. D., and Pokhilenko N. P. 2014. Jadeite in Chelyabinsk meteorite and the nature of an impact event on its parent body. *Scientific Reports* 4:5033.
- Presnall D. C. 1995. Phase diagrams of Earth-forming minerals. In *Mineral physics & crystallography: A handbook of physical constants*, edited by Ahrens T. J. Washington, D.C.: AGU. pp. 248–268.
- Remsberg A. R., Boland J. N., Gasparik T., and Liebermann R. C. 1988. Mechanism of the olivine-spinel transformation in Co_2SiO_4 . *Physics and Chemistry of Minerals* 15:498–506.
- Stanojević M. Z. V., Romčević N., and Stojanović B. 2007. Spectroscopic study of spinel ZnCr_2O_4 obtained from mechanically activated $\text{ZnO-Cr}_2\text{O}_3$ mixtures. *Journal of European Ceramics* 27:903–907.
- Stevens-Kalceff M. A. 2009. Cathodoluminescence microcharacterization of point defects in α -quartz. *Mineralogical Magazine* 73:585–605.
- Stöffler D., Keil K., and Scott R. D. E. 1991. Shock metamorphism of ordinary chondrites. *Geochimica et Cosmochimica Acta* 55:3845–3867.
- Tomioka N., and Fujino K. 1997. Natural $(\text{Mg,Fe})\text{SiO}_3$ -ilmenite and -perovskite in the Tenham meteorite. *Science* 277:1084–1086.
- Tomioka N., Mori H., and Fujino K. 2000. Shock-induced transition of $\text{NaAlSi}_3\text{O}_8$ feldspar into a hollandite structure in a L6 chondrite. *Geophysical Research Letters* 27:3997–4000.
- Tomioka N., Miyahara M., and Ito M. 2016. Discovery of natural MgSiO_3 tetragonal garnet in a shocked chondritic meteorite. *Science Advances* 2:e1501725.
- Walton E. and McCarthy S. 2017. Mechanisms of ringwoodite formation in shocked meteorites: Evidence from L5 chondrite Dhofar 1970. *Meteoritics & Planetary Science* 52:762–776.
- Wang A., Kuebler K. E., Jolliff B. L., and Haskin L. A. 2004. Raman spectroscopy of Fe-Ti-Cr-oxides, case study: Martian meteorite EETA79001. *American Mineralogist* 89:665–680.
- Wopenka B. and Pasteris J. D. 2005. A mineralogical perspective on the apatite in bone. *Materials Science and Engineering C* 25:131–143.
- Xie X., Minitti M. E., Chen M., Mao H.-K., Wang D., Shu J., and Fei Y. 2002. Natural high-pressure polymorph of merrillite in the shock veins of the Suizhou meteorite. *Geochimica et Cosmochimica Acta* 66:2439–2444.
- Xie X., Minitti M. E., Chen M., Mao H.-K., Wang D., Shu D., and Fei Y. 2003. Tuite, $\gamma\text{-Ca}_3(\text{PO}_4)_2$ a new mineral from the Suizhou L6 chondrite. *European Journal of Mineralogy* 15:1001–1005.
- Xie X., Chen M., and Wang C. 2011. Occurrence and mineral chemistry of chromite and xieite in the Suizhou L6 chondrite. *Science China Earth Science* 54:998–1010.
- Xie Z., Sharp T. G., and DeCarli P. S. 2006. High-pressure phases in a shock-induced melt vein of the Tenham L6 chondrite: Constraints on shock pressure and duration. *Geochimica et Cosmochimica Acta* 70:504–515.
- Zhang F. and Sekine T. 2007. Impact-shock behavior of Mg- and Ca-sulfates and their hydrates. *Geochimica et Cosmochimica Acta* 71:4125–4133.